mathematics

Article

An Integrated Probabilistic Imaging Damage Localization Method in Carbon Fiber-Reinforced Aluminum Laminate Considering Lamb Waves Propagation Characteristics

Bingquan Lu [1,2], Zhou Li [1,2,*], Yongming Wang [3] and Danfeng Zheng [4]

1 State Key Laboratory of Precision Manufacturing for Extreme Service Performance, Central South University, Changsha 410083, China; lubq2023@163.com
2 College of Mechanical and Electrical Engineering, Central South University, Changsha 410083, China
3 Xiangtan Quality Inspection Center for Industrial and Mining Electric Drive Vehicle, Xiangtan 411199, China; volt168@163.com
4 Automotive Engineering Research Institute, Byd Auto Industry Company Limited, Shenzhen 518000, China; zdf676360010@126.com
* Correspondence: lizhou_industry@hotmail.com

Abstract

Carbon fiber-reinforced aluminum laminate (CARALL) has excellent properties such as strong impact resistance and fracture toughness. Lamb waves are expected to provide an efficient means for non-destructive testing of CARALL. However, the complex propagation characteristics of Lamb waves in CARALL with both anisotropic and isotropic materials between layers make it difficult to accurately identify and locate the damage. We proposed an integrated probabilistic imaging method to detect the damage localization considering Lamb waves propagation characteristics. First, the relationship between the propagation velocity and direction of Lamb waves was analyzed. It was found that, unlike CFRP laminates, where Lamb waves propagate fastest along the transverse direction, Lamb waves in CARALL exhibit the highest velocity along the 45° direction. Subsequently, a damage localization algorithm considering anisotropy and integrated probability imaging was proposed. Experimental and numerical results demonstrate that the damage localization algorithm proposed in this work accurately predicted the location of damage in CARALL, and the area of damage could be characterized by the direct wave correlation coefficient of Lamb waves. This study provides a useful framework for non-destructive testing of CARALL.

Keywords: non-destructive testing; CARALL; Lamb waves; damage localization; propagation direction

MSC: 70B15; 74M15; 90C90

Received: 2 July 2026
Revised: 6 August 2026
Accepted: 10 August 2026
Published: 16 August 2026

1. Introduction

Composite materials are widely used in the aerospace, automotive industries and other fields because of their high strength, high stiffness and designability [1–4]. However, their applications are limited by their high price and low toughness. Fiber metal laminates are a new type of structure that combines high-strength fiber-reinforced composite materials with the high toughness of metals. The prices of steel and aluminum alloy are £0.30/kg and £1.36/kg, respectively, while the price of CFRP reaches £6.38/kg [5]. Fiber metal laminates combine the toughness and durability of metals with the superior fatigue and impact properties of FRP [6]. The most commonly used fiber metal laminates in industries such as aerospace are glass fiber-reinforced aluminum laminate (GLARE) [7], aramid fiber-reinforced aluminum laminate (ARALL) [8], and carbon fiber-reinforced aluminum laminate (CARALL) [9,10]. Compared with GLARE and ARALL, CARALL has received great attention due to its better lightweight advantage.

With the widespread application and extended service life of fiber metal laminates in key industrial fields, operational safety issues caused by damage and failure mechanisms, such as impact and fatigue, have become increasingly prominent [11,12]. The demand for fiber metal laminate health-monitoring and non-destructive testing technologies is increasing to monitor its health status in real time [13,14]. Non-destructive testing methods such as ultrasound, acoustic emission, X-ray, and thermal imaging can be used for damage detection of composites [15,16] and FML structures [6,17,18]. Ibarra Castanedo et al. [19] used infrared thermography to detect delamination and evaluate damage caused by impact in GLARE composite panels. Ultrasonic guided-wave (hereinafter referred to as guided-wave) testing is a commonly used method for non-destructive testing and health monitoring of fiber-reinforced composite material structures (including ultrasonic testing, acoustic emission, wavelet diagnostic technology, etc.), characterized by single-point excitation, small attenuation along the path, and high detection efficiency [20,21]. Recent studies have attempted to improve guided-wave-based monitoring methods by considering complex propagation behaviors, including physics-informed constraints, spatially varying wave velocities, temperature effects, and anisotropic propagation characteristics [22–25]. The real-time monitoring of damage and defects in carbon fiber-reinforced plastic using the interaction between ultrasonic guided waves and damage has achieved considerable progress [26].

When Lamb waves are used for damage localization and detection, transducers are usually distributed around a plate-shaped structure to form a network. When the actuator generates Lamb waves that propagate through the damaged area, part of the wave energy is scattered by the damage and received by the receiving transducers. Due to the anisotropy of carbon fiber-reinforced plastic and the strong wave attenuation, the propagation of Lamb waves in CARALL is relatively complex [27]. The parameters of composite materials, such as fiber volume fraction, layup sequence, and type of matrix/reinforcement material used, strongly affect the propagation characteristics of waves [28]. Waves in composite material laminate propagate at different velocities in various directions, and the shape of the wavefront varies with frequency. Hu et al. [29] proposed a damage localization algorithm based on pattern matching and verified the localization accuracy in composite material plates at different damage locations and fiber layers. Zhao et al. [30] evaluated interface debonding and low-speed impact damage in COPVs using laser ultrasonic guided waves.

Although Lamb waves have been effectively investigated in non-destructive testing of composite materials and metal laminates, their application to CARALL remains challenging because CARALL is composed of isotropic metal layers and anisotropic carbon fiber-reinforced plastic layers. The propagation characteristics of Lamb waves in two distinct materials are still unclear, and it is difficult to obtain accurate damage location information through existing damage localization algorithms. Mikhaylenko et al. [31] conducted a numerical study on the displacement field of such waves in a fiber metal laminate made of carbon fiber-reinforced plastic and steel by comparing analytical solutions and finite element models. Muc et al. [32] analyzed the dispersion curves obtained from numerical simulations and basic Lamb wave and shear horizontal elastic wave modes in fiber metal laminates. Rittmeier et al. [33] studied the effects of material interfaces and material impedance on the propagation of elastic waves in fiber metal laminates. Fattahi [34] evaluated delamination detection in FMLs by simulating Lamb wave propagation using a finite element (FE) model, and found that the phase velocity of S_0 Lamb wave mode was more sensitive to delamination damage than that of A_0 mode.

The coexistence of metal and carbon fiber-reinforced polymer layers in CARALL can significantly alter the wave velocity of guided waves, leading to errors in damage localization. Nevertheless, the propagation characteristics of guided waves in CARALL have received limited attention in previous studies. This paper establishes a damage parameter model for ultrasonic guided waves in CARALL. The proposed model can detect, locate, and characterize damage with high accuracy and minimal number of sensors.

The purpose of this study is to analyze the propagation characteristics of Lamb waves along different directions in CARALL, and propose a Lamb wave localization and damage quantification algorithm for CARALL. Accordingly, this study first analyzes the propagation characteristics of Lamb waves in CARALL and then proposes an integrated probabilistic imaging localization algorithm based on these characteristics. The relationship between Lamb wave characteristic parameters and damage location and severity is analyzed to establish a damage identification and quantification methods for CARALL.

2. The Guided-Wave Propagation Characteristics of CARALL

CARALL was made by alternately stacking aluminum alloy and CFRP layers, as shown in Figure 1a. The thickness of the CFRP layer is t_c, and the thickness of the metal layer is t_m. Due to the anisotropy of the CFRP layers, the propagation characteristics of Lamb waves in the laminate directly affect the location of damage. Therefore, in this section, the relationship between Lamb wave velocity and propagation direction is first analyzed.

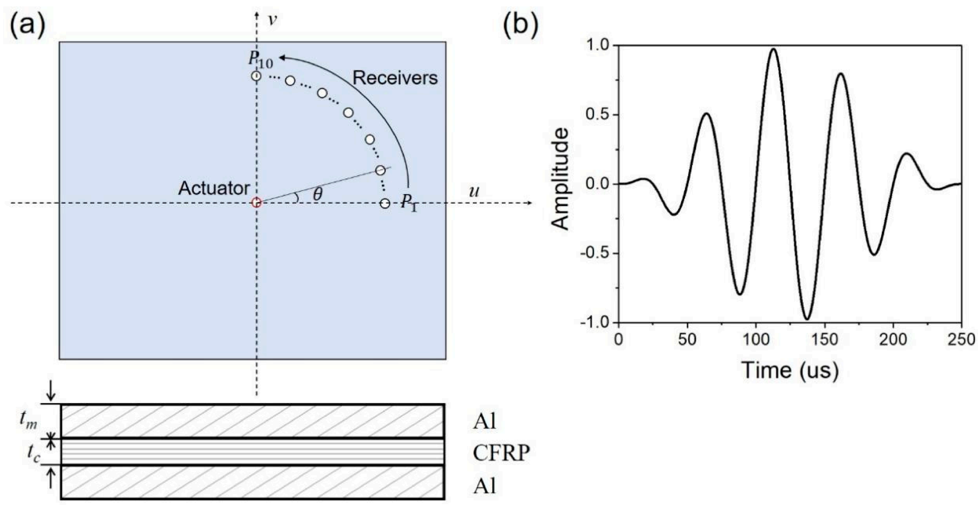

Figure 1. Simulation settings for Lamb wave propagation characteristics of CARALL: (**a**) PZT sensors layout; (**b**) excitation signal.

2.1. Establishment of Propagation Simulation Model of Guided Waves in CARALL

According to the theory of ultrasonic guided-wave propagation, the propagation characteristics of Lamb waves in anisotropic plates are determined using the Christoffel equation

$$\left(\Gamma_{il} - \rho v^2 \delta_{il}\right) U_l = 0,\ i, l = 1, 2, 3 \tag{1}$$

where ρ is the material density, U_l is the displacement field in the l-direction, v is the wave propagation velocity, and δ_{il} is the Kronecker delta. Christoffel second-order acoustic tensor

$\Gamma_{il} = C_{ijkl} n_j n_k$. C_{ijkl} is the elastic stiffness tensor of the material. For the CFRP layers, the elastic stiffness tensor is

$$C_{ijkl} = \begin{bmatrix} C_{11} & C_{12} & C_{12} & 0 & 0 & 0 \\ C_{12} & C_{11} & C_{12} & 0 & 0 & 0 \\ C_{12} & C_{12} & C_{11} & 0 & 0 & 0 \\ 0 & 0 & 0 & (C_{11}-C_{12})/2 & 0 & 0 \\ 0 & 0 & 0 & 0 & (C_{11}-C_{12})/2 & 0 \\ 0 & 0 & 0 & 0 & 0 & (C_{11}-C_{12})/2 \end{bmatrix} \quad (2)$$

It indicates that Lamb waves have the same propagation characteristics in all directions in metallic materials.

For CFRP layers with anisotropy, the elastic stiffness tensor is expressed in the material coordinates system (x, y, z) as

$$C_{ijkl} = \begin{bmatrix} C_{11} & C_{12} & C_{13} & 0 & 0 & 0 \\ C_{12} & C_{22} & C_{23} & 0 & 0 & 0 \\ C_{13} & C_{23} & C_{33} & 0 & 0 & 0 \\ 0 & 0 & 0 & C_{44} & 0 & 0 \\ 0 & 0 & 0 & 0 & C_{55} & 0 \\ 0 & 0 & 0 & 0 & 0 & C_{66} \end{bmatrix} \quad (3)$$

In the global coordinates (x′, y′, z′), the elastic stiffness tensor varies with the layup angle and can be obtained through the coordinate transformation

$$C_{mnst} = \beta_{mi}\beta_{nj}\beta_{sk}\beta_{tl}C_{ijkl} \quad (4)$$

The relationship between the coordinate transformation matrix and the laying angle is

$$\beta_{ab} = \begin{bmatrix} \cos\beta & \sin\beta & 0 \\ -\sin\beta & \cos\beta & 0 \\ 0 & 0 & 1 \end{bmatrix} \quad (5)$$

From Equations (3)–(5), the elastic stiffness tensor of the orthotropic CFRP layers varies with the layup angle β. Combined with Equation (1), the propagation velocity of Lamb waves is related to the layup angle.

Due to the stacking sequence of CFRP layers and aluminum alloy layers along the thickness direction in CARALL, the Lamb wave velocity cannot be directly obtained by substituting Equations (2) and (3) into Equation (1). Therefore, this study uses finite element simulation to calculate the propagation velocity of Lamb waves along different directions in CARALL.

The commercial software Abaqus/Explicit 2018 was used to simulate the wave propagation behavior of Lamb waves in CARALL, as shown in Figure 1a. The upper and lower layers of CARALL were made of aluminum alloy with a thickness of 0.2 mm, and the middle layer is made of CFRP. The stacking sequence was $[0/90]_4$, with a total of 8 layers, each with a thickness of 0.15 mm. The mesh was generated using C3D8R elements with a size of 1.0 mm. The mesh size was determined based on the wavelength criterion, and more than 10 elements were used per minimum wavelength to ensure accurate simulation of Lamb wave propagation [35]. The sampling frequency was set to 1.6×10^7 Hz, and the simulation duration was 0.0003 s. The properties of CFRP are listed in Table 1. The density and Young's modulus of aluminum alloy are 2.7×10^3 kg/m^3 and 69 GPa, respectively [12]. The sine signal modulated by a Hanning window with a frequency of 200 kHz was applied in the center of laminates, as shown in Figure 1b, and the expression of the function was given in Equation (6). PZT receivers were placed in different directions at a distance of 40 mm from the center.

$$A = \frac{1}{2}\left[1 - \cos\left(\frac{2\pi f_c t}{n}\right)\sin(2\pi f_c t)\right] \quad (6)$$

Table 1. Material parameters of CFRP [12].

Parameters	Values
Density	ρ = 1570 kg/m^3
Elastic	E_1 = 128,000 MPa, E_2 = 8800 MPa, E_3 = 8800 MPa, υ_{21} = 0.357, G_{12} = 3147 MPa
Strength	X_T = 1373 MP, X_C = 718 MPa, S = 51.92 MPa Y_T = 24 MPa, Y_C = 121 MPa, S = 51.92 MPa

2.2. Comparison of Propagation Characteristics in CFRP Laminates, Aluminum Alloy Plate, and CARALL

The propagation characteristics of isotropic aluminum alloy plates, anisotropic CFRP laminates, and anisotropic/isotropic CARALL are compared and shown in Figure 2. From Figure 2a,d, Lamb waves propagate in the aluminum alloy plate along all directions at the same velocity, while the CFRP laminate exhibits obvious anisotropy: Lamb waves have faster propagation velocity along the 0° and 90° directions, while the propagation velocity is lower along the 45° direction. This is because the stacking sequence of the CFRP laminate is $[0/90]_4$, which means that the propagation velocity is higher along the fibers. It is evident that dispersion behavior is more pronounced along the 45° direction than in the other directions, as shown in Figure 2e.

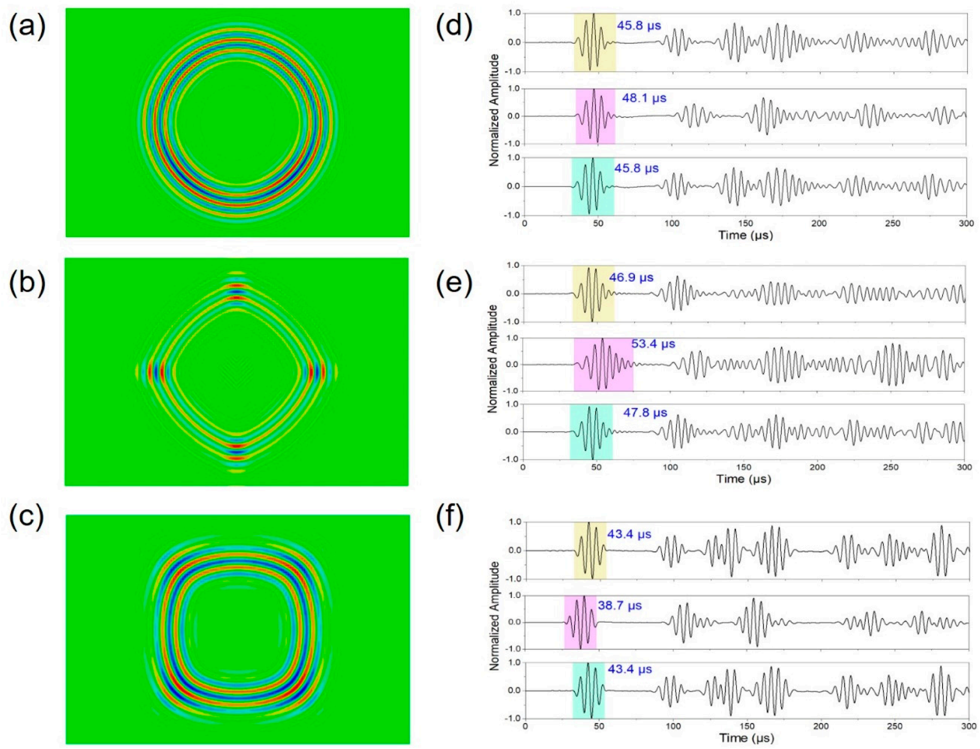

Figure 2. Lamb wave propagation characteristics in different laminates: (**a**–**c**) deformation contour maps of aluminum alloy plates, CFRP laminate, and CARALL, respectively; (**d**–**f**) signals received by PZT sensors at points P_0, P_5, and P_{10}, respectively.

https://doi.org/10.3390/math14162961

Compared with aluminum alloy plates and CFRP laminates, CARALL has the slowest propagation velocity along the 0° and 90° directions, but the fastest propagation velocity along approximately the 45° direction. This is the result of the combined effects of two different materials (aluminum alloy and CFRP) and the stacking sequence. To quantitatively characterize the propagation characteristics in the above directions, the wavelet transform method was applied to the signals at the excitation point and at each receiving point to obtain the signal envelope, as shown in Figure 3a. The time difference between the first peaks of the wave packet at the excitation and receiving point is the time of flight (ToF) of the Lamb wave. The group velocity is the ratio of the distance between the receiving point and the excitation point to the time of flight. The group velocities of the CFRP laminate and CARALL in all directions were normalized, and the characteristics are shown in Figure 3b. It can be seen that the propagation velocity of CFRP laminates reaches its maximum value in the 90° direction, whereas the maximum velocity of CARALL occurs in the 45° direction.

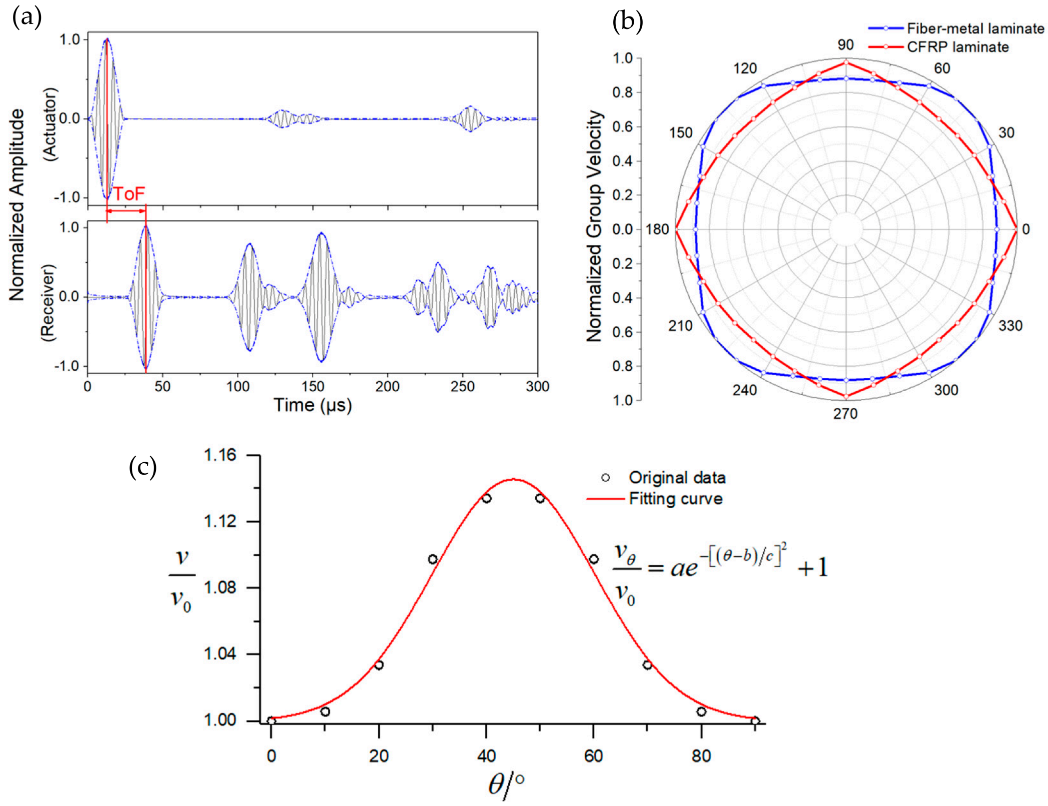

Figure 3. Calculation of propagation velocity of Lamb waves in CARALL: (**a**) acquisition of flight time; (**b**) group velocity in all directions; (**c**) the fitting of group velocity.

For the [0/90] CFRP laminate, the effective stiffness along an arbitrary propagation direction is determined by the transformed stiffness matrix due to the misalignment between the material principal axes and the wave propagation direction. At approximately 45°, the coupling between normal and shear deformation components becomes the most significant, resulting in enhanced coupling stiffness terms (e.g., Q_{16} and Q26) and increased effective in-plane stiffness. For CARALL, the introduction of aluminum layers further modifies the stiffness distribution, as the combined contribution of the anisotropic CFRP plies and the isotropic aluminum layers changes the overall stiffness along the 45° direction, leading to a higher guided-wave propagation velocity.

The relationship between the group velocity and propagation angle of guided waves is:

$$\frac{v_\theta}{v_0} = ae^{-[(\theta-b)/c]^2} + 1 \tag{7}$$

where v_0 is the horizontal propagation velocity, and b and c are the fitting parameters.

The normalized velocity variations are listed in Table 2, and the fitting results indicate that the parameters a = 0.1458, b = 45, c = 21.4516 in Equation (7).

Table 2. Normalized velocity variations with ply angle.

$\theta/°$	0	10	20	30	40	50	60	70	80	90
v_θ/v_0	1	1.0057	1.0339	1.0975	1.1343	1.1343	1.0975	1.0339	1.0057	1

3. Integrated Probabilistic Imaging Damage Localization Algorithm Based on Anisotropic Propagation

According to Bayes' theorem [36], when the damage time D occurs, the posterior probability of damage occurring at α is

$$p(\boldsymbol{\alpha}|\boldsymbol{D}) \propto p(\boldsymbol{D}|\boldsymbol{\alpha})p(\boldsymbol{\alpha}) \tag{8}$$

where $p(\boldsymbol{\alpha})$ represents the prior probability. It can be obtained through the probabilistic diagnostic imaging, and $p(\boldsymbol{D}|\boldsymbol{\alpha})$ can be obtained through the elliptical trajectory method.

As shown in Figure 4, guided waves are excited at the excitation point and propagate with a propagation angle θ_{d1}, where they are scattered by the damaged area. The scattered signal propagates along a path with an angle of θ_{d2} and reaches the receiving sensor. The total propagation time is

$$\frac{\sqrt{(x-x_a)^2+(y-y_a)^2}}{v_g(\theta_{d1})} + \frac{\sqrt{(x-x_a)^2+(y-y_a)^2}}{v_g(\theta_{d2})} = ToF \tag{9}$$

where $(x_a,\ y_a)$ are the coordinates of the excitation point, and $(x_r,\ y_r)$ are the position coordinates of the receiving point. From Equations (1) and (2), we can obtain

$$\frac{\sqrt{(x-x_a)^2+(y-y_a)^2}}{ae^{-[(\theta_{d1}-b)/c]^2}+1} + \frac{\sqrt{(x-x_a)^2+(y-y_a)^2}}{ae^{-[(\theta_{d2}-b)/c]^2}+1} = v_0 \cdot T_a \tag{10}$$

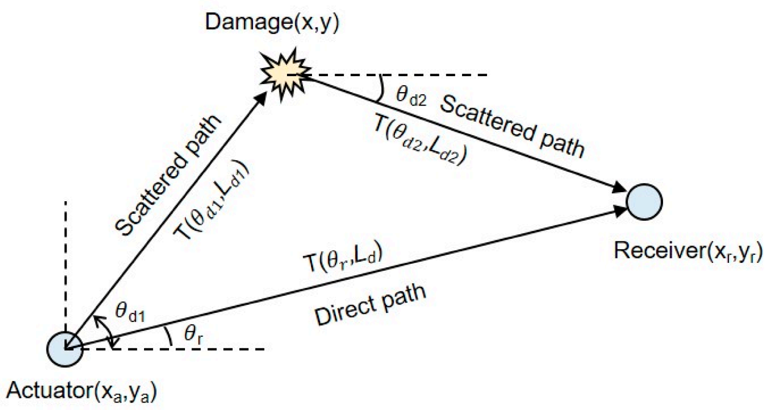

Figure 4. Schematic diagram of Lamb wave propagation process.

The angles can be calculated based on the coordinates.

$$\theta_{d1} = ac\tan(\frac{y-y_a}{x-x_a})\ \theta_{d2} = ac\tan(\frac{y_r-y}{x_r-x}) \quad (11)$$

The maximum likelihood function can be represented by the following equation:

$$p\left(D\middle|\boldsymbol{\alpha},\boldsymbol{\sigma}^2\right) = \frac{1}{\left(\sqrt{2\pi}\sigma\right)^{N/2}}\exp\left\{-\frac{1}{2\sigma^2}\sum_{i=1}^{N}[T(x,y)-T_a(x_d,y_d)]^2\right\} \quad (12)$$

Then, the prior probability is calculated. The guided waves interact with the damage. The correlation coefficient between damage-guided waves and the baseline signal is

$$\rho = \frac{\sum_{i=1}^{n}\left(h_i-\overline{h}\right)\left(d_i-\overline{d}\right)}{\sqrt{\sum_{k=1}^{K}\left(h_i-\overline{h}\right)^2}\sqrt{\sum_{k=1}^{K}\left(d_i-\overline{d}\right)^2}} \quad (13)$$

where h_i and d_i are the response signals measured from CARALL when it is in an undamaged and damaged condition, respectively. The first wave packet of each received signal is selected to calculate the correlation coefficient between the two signals.

Assuming that the load decreases with space, the relationship between the probability of damage at the reconstructed position (x, y) and the correlation coefficient is

$$p(\boldsymbol{\theta}) = p(x,y) = \frac{1}{N}\sum_{i=1}^{N}(1-\rho_i)w_i(x,y) \quad (14)$$

where the weight coefficients $w_i(x,y)$ can be represented by piecewise functions, where the weight coefficients gradually decrease as the distance between the two points increases. When the distance exceeds the threshold, the weight coefficient is set to zero.

$$w_i(x,y) = \begin{cases} 1-\frac{1}{\beta}RD_i(x,y), & RD_i(x,y) < \beta \\ 0 & RD_i(x,y) \geq \beta \end{cases} \quad (15)$$

where RD_i is expressed as

$$RD_i(x,y) = \frac{\sqrt{(x_i-x_{ai})^2+(y_i-y_{ai})^2}+\sqrt{(x_i-x_{ri})^2+(y_i-y_{ri})^2}}{\sqrt{(x_{ri}-x_{ai})^2+(y_{ri}-y_{ai})^2}} \quad (16)$$

By substituting Equations (12) and (14) into Bayes' theorem given in Equation (8), the posterior probability distribution of damage can be calculated

$$p(\boldsymbol{\alpha}|\boldsymbol{D}) \propto \frac{1}{\left(\sqrt{2\pi}\sigma\right)^{N/2}}\exp\left\{-\frac{1}{2\sigma^2}\sum_{i=1}^{N}[T(x,y)-T_a(x_d,y_d)]^2\right\}\cdot\frac{1}{N}\sum_{i=1}^{N}(1-\rho_i)w_i(x,y) \quad (17)$$

Therefore, the probability of damage at different positions in space can be calculated by Equation (17). The formula obtained by the Bayes' theorem mentioned above is very complex and can be sampled using the Markov Chain Monte Carlo (MCMC) algorithm. The algorithm process is listed as follows.

Step 1: Set the iteration number NT and the initial state of the random parameters $(\mathrm{x}_0, \mathrm{y}_0, \sigma_0)$.

Step 2: Sample x^* from the conditional probability distribution and generate u ~ U (0, 1) from the uniform distribution.

Step 3: Choose the normal distribution transition matrix Q, if $u < \min\left(\frac{p(j)Q(j,i)}{p(i)Q(i,j)}, 1\right)$, accept sampling x^*, then accept —> t = 1 $x_1 = x^*$. Otherwise, when $t = 1$, $x_1 = x_0$.

Step 4: Repeat Step 2 and Step 3 until the iteration count NT is reached.

Although the MCMC algorithm requires iterative sampling and may introduce additional computational cost, it provides a probabilistic framework for damage localization and uncertainty quantification. The computational efficiency can be further improved through sampling strategy optimization and parallel computation. Therefore, the proposed method shows potential for practical structural health monitoring applications, while real-time implementation requires further investigation.

4. Simulation Analysis and Experimental Verification

4.1. Simulation Analysis

To verify the damage localization method for CARALL considering anisotropic characteristics, the finite element method was used to simulate the guided-wave response, and the simulation design was the same as that described in Section 2.1. Delamination was introduced into the middle of the CARALL, and the sensor arrangement and the location of the damage are shown in Figure 5a. Four sensors were placed on the rectangular laminate. The delamination was set at (20 mm, 15 mm) and located within the CFRP layer between the aluminum alloy plates. The time-domain signals of S1 and S4, as well as the frequency-domain signals obtained through wavelet transform, are shown in Figure 5b. For S1, a signal reflected from the boundary is received after approximately 84.5 µs. For S4, a direct wave signal generated by excitation at S1 was first received at 85.7 µs.

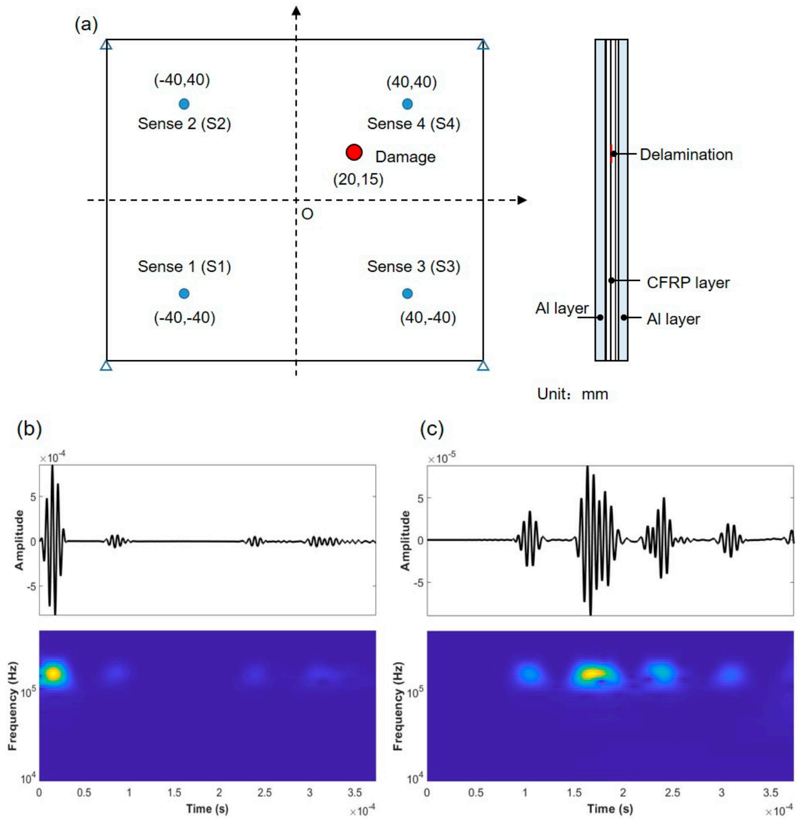

Figure 5. Detection of delamination: (**a**) model settings; (**b**) Lamb wave response signals (sensor 1–sensor 4) under healthy and damaged states; (**c**) comparison of the first wave packets.

A 200 kHz narrowband five-period sine signal modulated by a Hanning window using a concentrated force is applied. Lamb waves responses under both healthy and damaged conditions are obtained, as shown in Figure 5b,c.

The Lamb wave response signals along the six paths, including S1–S2, S1–S3, and other sensor paths are extracted. The TOF values of different signals are calculated, and the correlation coefficients are obtained using Equation (13), as listed in Table 3. It can be seen that the correlation coefficient for the S1–S4 path is the smallest, indicating that the damage is located near the propagation path between S1 and S4, which is consistent with the setting of damage location.

Table 3. Time of flight and correlation coefficient of different propagation paths.

Path	S1–S2	S1–S3	S1–S4	S2–S3	S2–S4	S3–S4
TOF (s)	8.78×10^{-5}	8.78×10^{-5}	7.35×10^{-5}	9.13×10^{-5}	6.78×10^{-5}	6.46×10^{-5}
ρ_{ij}	1	1	0.9619	0.9997	0.9999	0.9991

A program is written in MATLAB R2021a to calculate the probability of damage at different locations using Equation (10), and obtain the probability distribution in spatial location using the MCMC algorithm, as shown in Figure 6a. The maximum probability of damage is obtained at (18.5 mm, 16.2 mm), which is very close to the actual damage location (20 mm, 15 mm), as listed in Table 4.

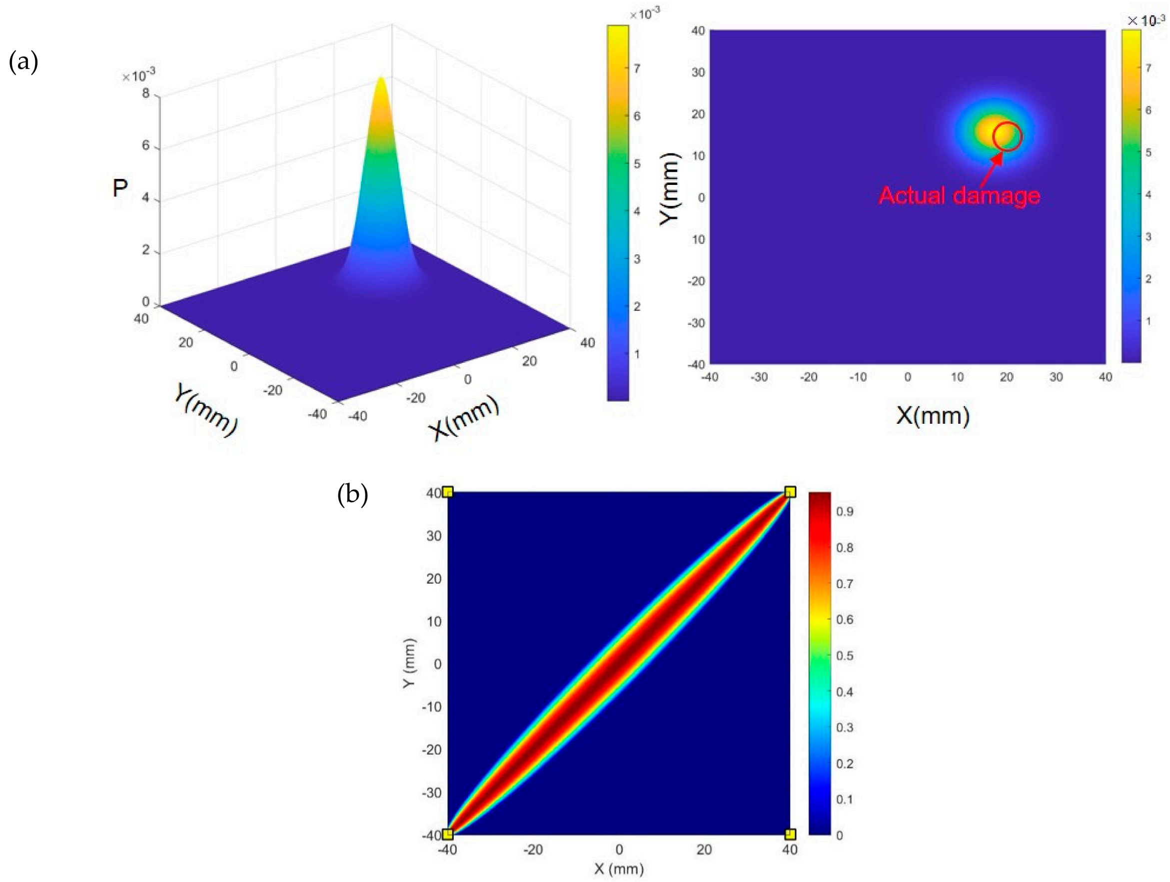

Figure 6. Results of: (**a**) damage localization algorithm proposed in this word; (**b**) traditional probability damage imaging.

Table 4. Comparison of predicted vs. actual coordinates.

Actual Coordinates	Predicted Coordinates	Errors
(20 mm, 15 mm)	(18.5 mm, 16.2 mm)	(1.5 mm, −1.2 mm)

The result of the conventional probability-based damage imaging (PDI) method is shown in Figure 6b. In the conventional PDI method, the damage probability is calculated only using Equation (18). The results indicate that the damage is distributed along the S1–S4 sensing path, which is consistent with the actual damage location. However, due to the limited number of sensors, accurate damage localization cannot be achieved because of insufficient elliptical intersections.

$$P(x,y) = \sum_{i=1}^{N} (1-\rho_i) w_i(x,y) \tag{18}$$

In practical applications, the stacking sequence may not be identical to that considered in this study due to requirements related to structural strength and stiffness. Since the propagation velocity v_θ is dependent on the ply angle, a similar methodology can be employed to establish the velocity relationship for different laminate configurations and further integrate it into the localization method.

To further explore the damage size estimation method based on Lamb waves, finite element models with different damage radii were established. Using the same method, the differential signals on the path S1–S4 with the minimum correlation coefficient were obtained, as shown in Figure 7. The relationship between the damage index $e = 1 - \rho$ and the damage radius was calculated, and the index increased as the damage radius increased. The relationship between the damage radius and the damage index was obtained by fitting a quadratic function. As shown in Figure 7, the coefficient of determination R^2 was 0.99536, indicating that the fitting accuracy is high and the corresponding damage radius could be obtained through the correlation coefficient. The present study only considers circular delamination damage. However, damage in practical structures usually exhibits more complex geometries. Therefore, further experimental investigations, numerical simulations, and advanced damage imaging approaches are required to accurately characterize the actual damage shape. The response for damaged and undamaged CARALL is shown in Figure 8.

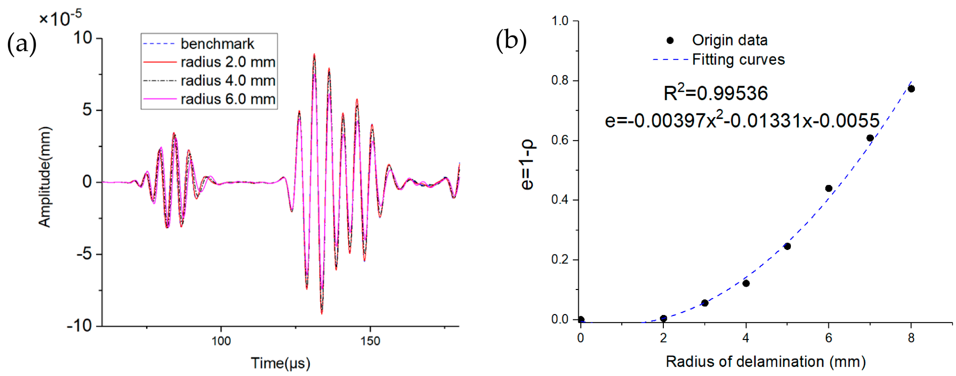

Figure 7. Response of different damage radii of CARALL: (**a**) time domain signal; (**b**) damage indicators.

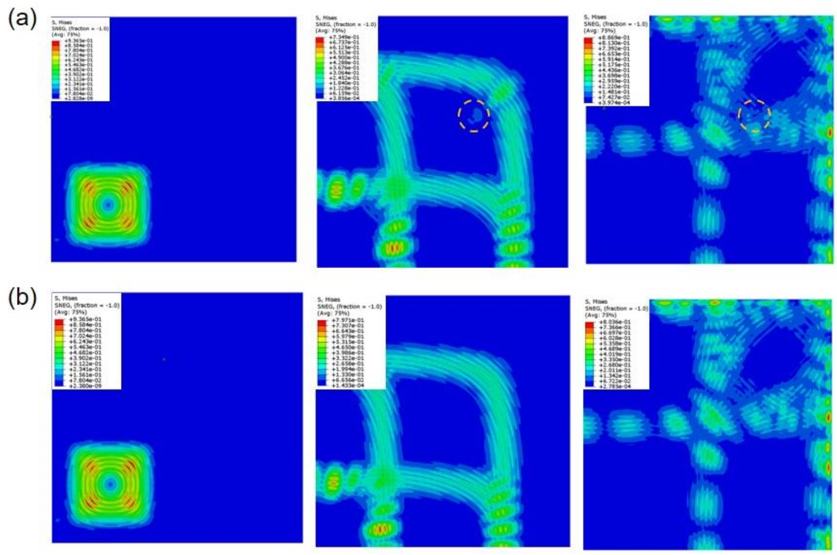

Figure 8. Comparison of Lamb wave response for (**a**) damaged and (**b**) undamaged CARALL.

4.2. Experiment Validation

The feasibility of the proposed algorithm was further verified through Lamb wave experiments. The Lamb wave detection system used in this study is shown in Figure 9. A computer was used to control the function generator to generate high-energy pulse signals. The signals were amplified by a power amplifier to produce high-voltage excitation signals, which were applied to the CARALL specimen through piezoelectric transducers. At the receiving end, the received signal is converted into an electrical signal through piezoelectric ceramics and input into the oscilloscope. The function generator and oscilloscope are manufactured by Puyuan Company (Suzhou, China), with models DG2052 and DHO1074, respectively. The power amplifier was an ATA−2021B produced by Antai Electronic Technology Company (Xi'an, China). The probe end adopts a full electrode piezoelectric ceramic with a diameter of 5.0 mm and a thickness of 0.3 mm. The signals were sampled after the system reached a stable operating condition, with a sampling frequency of 2×10^6 Hz. The recording duration was 3.0×10^{-4} s. The digital filtering and noise processing settings were kept as the default parameters of the DHO1074 oscilloscope.

A function generator was controlled by a computer to generate a five-cycle sinusoidal signal with a central frequency of 200 kHz. The signal is modulated by a Hanning window function and applied through the piezoelectric transducer. After passing through the CARALL, the Lamb wave signal is received and displayed on an oscilloscope.

Response signals are obtained through data collection systems in both healthy and damaged states of CARALL, as shown in Figure 10. The channel information from the paths is collected and to obtained scattered signals. As can be seen, the excitation signal of the power amplifier is basically the same as the simulation results. After propagating through the laminate, the receiving transducer detects the direct Lamb wave signal. Afterwards, the Lamb wave continued to propagate forward until it was reflected from the boundary of the CARALL. A clear reflected signal was detected by the receiving transducer, which confirms the validity of the previous simulation analysis. A stronger scattering signal is generated on the S1–S4 path, and the correlation coefficient between the two signals is relatively small, indicating that the damage is closer to this path and farther from other paths.

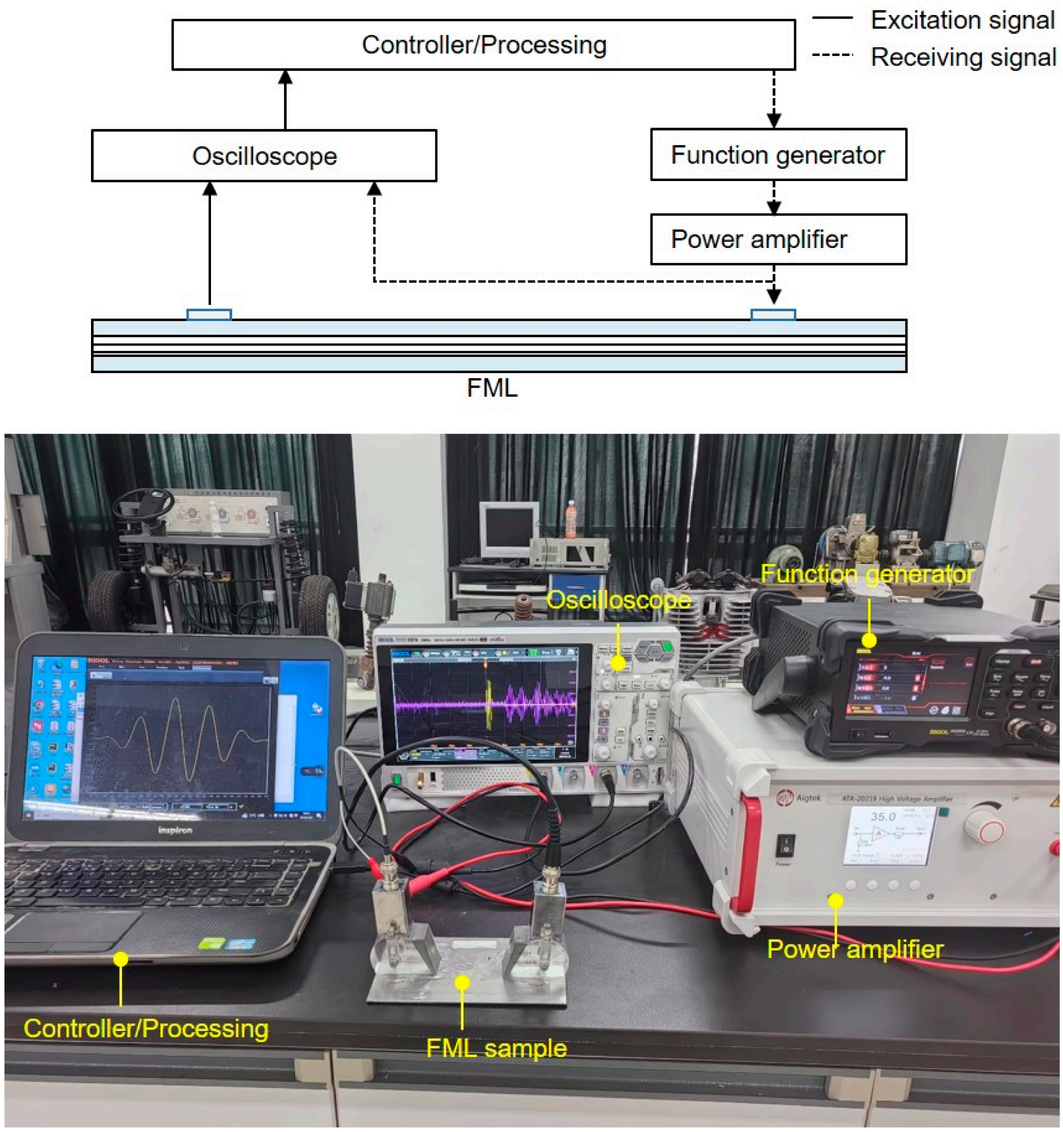

Figure 9. Establishments of the tests.

The time of flight and correlation coefficients on different paths were calculated using the proposed algorithm, and the spatial distribution of damage probability was plotted using the MCMC algorithm, as shown in Figure 11. The results showed that the maximum damage probability was located at (−2 mm, −2 mm) and gradually decreased away from this location, which was very close to the damage location (0, 0). These results demonstrate that the proposed algorithm in this paper can accurately localize the damage location. The error may be due to instrument noise and other reasons, which introduced deviations in the extracted ToF values and correlation coefficients from their ideal values. In summary, the damage location of CARALL can be accurately identified and located using the method proposed in this work.

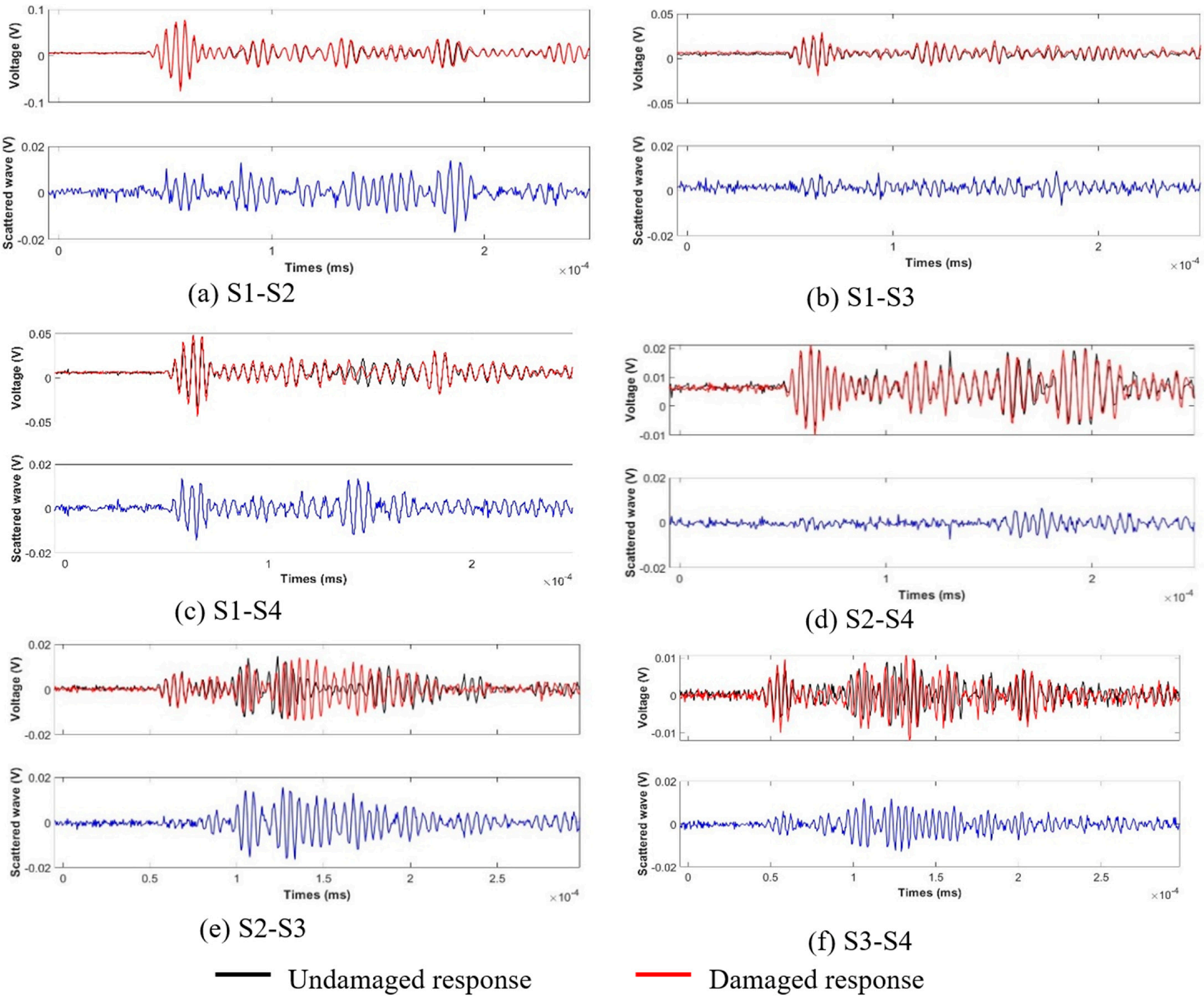

Figure 10. Lamb waves and its scattered waves of the CARALL tests.

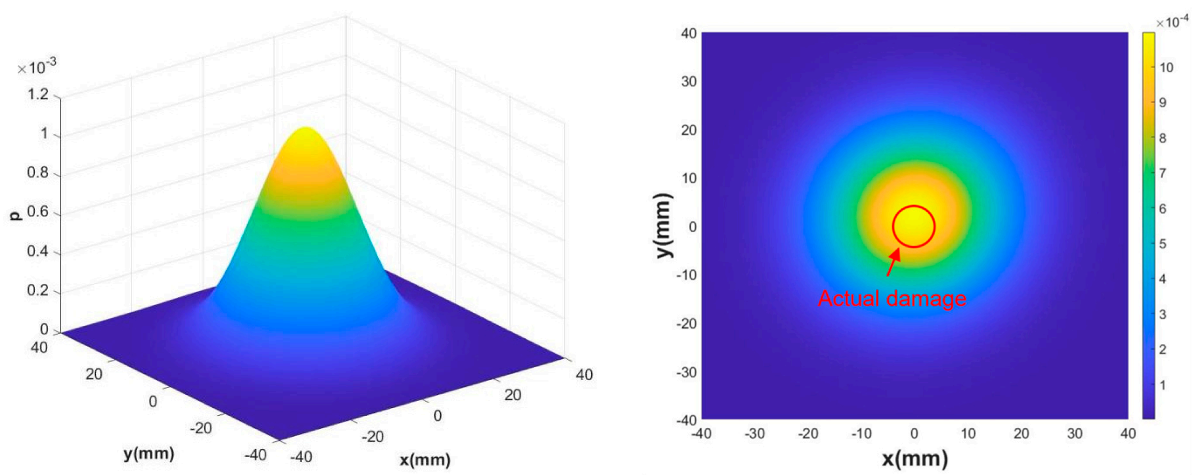

Figure 11. Results of damage location algorithm in experimental tests.

To verify the stability of the proposed method, the influence of measurement noise on the correlation coefficient of the S2–S3 path was investigated under different signal-to-noise ratios (SNRs) of 10, 20, and 30 dB. The results show that the correlation coefficient remains 0.9451 for all three SNR levels. Similarly, different time windows with the same duration of 25 μs were selected to calculate the correlation coefficient of the S2–S3 path, and the results are presented in Table 5. When the starting time of the window was shifted from 45 μs to 60 μs, the variation in the correlation coefficient was only 0.0314. Therefore, the influence of noise level and time-window selection on the localization results can be considered negligible.

Table 5. Effect of different time-window positions on the correlation coefficient of the S2–S3 path.

Time window (μs)	45–70	50–75	55–80	60–85
ρ	0.943	0.9451	0.9347	0.9116

5. Conclusions

This paper studies the Lamb wave propagation characteristics and damage localization method for CARALL. First, the characteristics of CARALL in different propagation directions are analyzed and compared with those of CFRP laminate and aluminum plate. Then, an integrated probabilistic damage localization method considering anisotropic propagation characteristics is proposed. Finally, the damage localization method is evaluated and verified through simulations and experiments. The key conclusions are listed as follows:

(1) The propagation velocity of CFRP laminates reaches its maximum along the 90° direction, while that of CARALL reaches its maximum along approximately the 45° direction.
(2) An evaluation index characterizing the damage radius was proposed, and an empirical formula for the relationship between the index and the damage radius was obtained.
(3) Based on the Bayesian formula, an integrated probabilistic damage localization method was proposed, which accurately located the damage position in CARALL, and the accuracy of the localization method was verified through numerical simulations and experiments. The damage localization errors were within 2.0 mm compared with the actual damage locations.

The proposed method is currently validated for the investigated CARALL structure with a single damage case. Its applicability to different reinforcement configurations, multiple concurrent damages, complex geometries, and varying operational conditions requires further investigation. Future work will focus on establishing a more general group velocity prediction model for various CARALL configurations and extending the proposed method to more complex damage scenarios.

Author Contributions: Conceptualization, B.L. and Z.L.; methodology, B.L. and D.Z.; validation, B.L. and Z.L.; formal analysis, B.L. and Y.W.; investigation, B.L. and Y.W.; resources, B.L. and Y.W.; data curation, B.L.; writing—original draft, B.L.; writing—review and editing, B.L., Z.L. and D.Z.; visualization, B.L.; supervision, B.L. and Y.W.; project administration, Z.L.; funding acquisition, B.L. All authors have read and agreed to the published version of the manuscript.

Funding: This research was funded by National Natural Science Foundation of China, Grant number 52505165, the Project of State Key Laboratory of Precision Manufacturing for Extreme Service Performance, Central South University, Grant number ZZYJKT2025−07, by the Open Fund of the National Key Laboratory of Advanced Off-Road System Technology, Grant number KF20250016C. by the Natural Science Foundation of Hunan Province, Grant number 2025JJ80227, 2026JJ60429. This work was supported in part by the High Performance Computing Center of Central South University.

Institutional Review Board Statement: Not applicable.

Informed Consent Statement: Not applicable.

Data Availability Statement: The original contributions presented in this study are included in the article. Further inquiries can be directed to the corresponding author.

Conflicts of Interest: Author Yongming Wang was employed by the company Xiangtan Quality Inspection Center for Industrial and Mining Electric Drive Vehicle. Author Danfeng Zheng was employed by the company Automotive Engineering Research Institute, Byd Auto Industry Company Limited. The remaining authors declare that the research was conducted in the absence of any commercial or financial relationships that could be construed as a potential conflict of interest.

References

1. Kazemianfar, B.; Nami, M.R. Influence of oblique low velocity impact on damage behavior of 2D and 3D woven composites: Experimental and numerical methods. *Thin-Walled Struct.* **2021**, *167*, 108253. [CrossRef]
2. Zhang, L.; Sun, J.; Wang, W.; Shi, M.; Rui, X.; Zhang, H. Research on delamination damage imaging of CFRP laminate based on laser ultrasonic guided waves. *Measurement* **2026**, *265*, 120379. [CrossRef]
3. Tian, T.; Liu, W.; Yang, H.; Yang, Z.; Xu, H.; Yang, L.; Wu, Z. Spatiotemporal parallel network for damage localization regression in carbon fiber reinforced composite plates using multifrequency guided waves. *Measurement* **2025**, *257*, 118495. [CrossRef]
4. Rezasefat, M.; Gonzalez-Jimenez, A.; Giglio, M.; Manes, A. Numerical study on the dynamic progressive failure due to low-velocity repeated impacts in thin CFRP laminated composite plates. *Thin-Walled Struct.* **2021**, *167*, 108220. [CrossRef]
5. Meredith, J.; Bilson, E.; Powe, R.; Collings, E.; Kirwan, K. A performance versus cost analysis of prepreg carbon fibre epoxy energy absorption structures. *Compos. Struct.* **2015**, *124*, 206–213. [CrossRef]
6. Yamada, K.; Kötter, B.; Nishikawa, M.; Fukudome, S.; Matsuda, N.; Kawabe, K.; Fiedler, B.; Hojo, M. Mechanical properties and failure mode of thin-ply fiber metal laminates under out-of-plane loading. *Compos. Part A Appl. Sci. Manuf.* **2021**, *143*, 106267. [CrossRef]
7. El-Baky, M.A.A.; Attia, M.A. The mechanical performance of the laminated aluminum-epoxy/glass fiber composites containing halloysite nanotubes: An experimental investigation. *J. Ind. Text.* **2022**, *51*, 8690S–8737S. [CrossRef]
8. Maryan, M.S.; Ebrahimnezhad-Khaljiri, H.; Eslami-Farsani, R. The experimental assessment of the various surface modifications on the tensile and fatigue behaviors of laminated aluminum/aramid fibers-epoxy composites. *Int. J. Fatigue* **2022**, *154*, 106560. [CrossRef]
9. Üstün, T.; Saraloğlu Güler, E. Enhancing carbon fiber reinforced aluminum laminates with cellulose paper interlayers: Experimental characterization of tensile, flexural, and interlaminar fracture toughness. *Compos. Interfaces* **2024**, *31*, 1225–1245. [CrossRef]
10. Mahesh, V. Comparative study on low velocity impact response of carbon-fiber-reinforced polymer/thermoplastic elastomer based fiber metal laminates with and without interleaving of elastomeric layer. *J. Thermoplast. Compos. Mater.* **2024**, *37*, 604–624. [CrossRef]
11. Zhang, J.Y.; Lu, B.; Zheng, D.; Li, Z. Experimental and numerical study on energy absorption performance of CFRP/aluminum hybrid square tubes under axial loading. *Thin-Walled Struct.* **2020**, *155*, 106948. [CrossRef]
12. Lu, B.; Zhang, J.; Zheng, D.; Zhang, T.; Xie, J. Study on off-center impact behavior and damage characterization of carbon fiber reinforced aluminum laminate. *Compos. Struct.* **2023**, *304*, 116404. [CrossRef]
13. Guo, S.; Rebillat, M.; Mechbal, N. Dichotomy property of dispersion equation of guided waves propagating in anisotropic composite plates. *Mech. Syst. Signal Process.* **2022**, *164*, 108212. [CrossRef]
14. Liu, W.; Hu, J.; Lv, F.; Tang, Z. A new method for long-term temperature compensation of structural health monitoring by ultrasonic guided wave. *Measurement* **2025**, *252*, 117310. [CrossRef]
15. Gao, Y.; Sun, L.; Song, R.; Peng, C.; Wu, X.; Wei, J.; Jiang, M.; Sui, Q.; Zhang, L. Damage localization in composite structures based on Lamb wave and modular artificial neural network. *Sens. Actuators A Phys.* **2024**, *377*, 115644. [CrossRef]
16. Gonzalez-Jimenez, A.; Lomazzi, L.; Junges, R.; Giglio, M.; Manes, A.; Cadini, F. Enhancing Lamb wave-based damage diagnosis in composite materials using a pseudo-damage boosted convolutional neural network approach. *Struct. Health Monit.* **2024**, *23*, 1514–1529. [CrossRef]
17. Jakubczak, P.; Nardi, D.; Bieniaś, J.; Sinke, J. Non-destructive testing investigation of gaps in thin Glare laminates. *Nondestruct. Test. Eval.* **2021**, *36*, 17–34. [CrossRef]
18. Montinaro, N.; Cerniglia, D.; Pitarresi, G. Flying laser spot thermography technique for the NDE of fibre metal laminates disbonds. *Compos. Struct.* **2017**, *171*, 63–76. [CrossRef]
19. Ibarra-Castanedo, C.; Avdelidis, N.P.; Grinzato, E.G.; Bison, P.G.; Marinetti, S.; Plescanu, C.C.; Bendada, A.; Maldague, X.P. Delamination detection and impact damage assessment of GLARE by active thermography. *Int. J. Mater. Prod. Technol.* **2011**, *41*, 5–16. [CrossRef]

20. Wu, J.; Xu, X.; Liu, C.; Deng, C.; Shao, X. Lamb wave-based damage detection of composite structures using deep convolutional neural network and continuous wavelet transform. *Compos. Struct.* **2021**, *276*, 114590. [CrossRef]
21. De Luca, A.; Perfetto, D.; De Fenza, A.; Petrone, G.; Caputo, F. Guided wave SHM system for damage detection in complex composite structure. *Theor. Appl. Fract. Mech.* **2020**, *105*, 102408. [CrossRef]
22. Nie, Q.; Zhang, J.; Wang, Y.; Wang, D.; Wang, Q.; Shi, Y.; Wang, C. Physics-Informed Machine Learning for Predicting Stress Wave Transmission Across Realistic Rock Joints. *IEEE Access* **2025**, *13*, 212735–212744. [CrossRef]
23. Zhang, X.; Fan, C.; Yang, J.; Yong, Z. Adaptive compensated MUSIC beamforming for Lamb wave damage localization under varying temperature. *Struct. Health Monit.* **2026**, 14759217261460034. [CrossRef]
24. Hu, S.; Zhai, G.; Lu, C.; Li, Z. Defect localization in switch rail foot with variable width via spatial mapping of SH0-like guided wave time-of-flight. *NDT E Int.* **2026**, *162*, 103743. [CrossRef]
25. Li, X.; Li, C.; Wang, S.; He, J.; Li, Z. Electromagnetic ultrasonic measurement method for axial force of bolts with non-uniform temperature distribution. *NDT E Int.* **2026**, *162*, 103749. [CrossRef]
26. Fathi, H.; Kazemirad, S.; Nasir, V. Mechanical degradation of wood under ultraviolet radiation characterized by Lamb wave propagation. *Struct. Control. Health Monit.* **2021**, *28*, e2731. [CrossRef]
27. Kudela, P.; Ostachowicz, W.; Żak, A. Damage detection in composite plates with embedded PZT transducers. *Mech. Syst. Signal Process.* **2008**, *22*, 1327–1335. [CrossRef]
28. Pant, S.; Laliberte, J.; Martinez, M.; Rocha, B. Derivation and experimental validation of Lamb wave equations for an n-layered anisotropic composite laminate. *Compos. Struct.* **2014**, *111*, 566–579. [CrossRef]
29. Hu, C.; Fu, X.; Yuan, Y.; Xiao, B.; Sun, M.; Yang, B. A novel damage localization technique for type III composite pressure vessels based on guided wave mode-matching method. *Compos. Struct.* **2024**, *346*, 118414. [CrossRef]
30. Zhao, J.; Yang, L.; Wang, H.; Zhao, J.; Li, N.; Chang, L.; Ji, H.; Qiu, J. Laser-Generated Guided Waves for Damage Detection in Metal-Lined Composite-Overwrapped Pressure Vessels. *Polymers* **2022**, *14*, 3823. [CrossRef] [PubMed]
31. Mikhaylenko, A.; Rauter, N.; Bellam Muralidhar, N.K.; Barth, T.; Lorenz, D.A.; Lammering, R. Numerical analysis of the main wave propagation characteristics in a steel-cfrp laminate including model order reduction. *Acoustics* **2022**, *4*, 517–537. [CrossRef]
32. Muc, A.; Barski, M.; Stawiarski, A.; Chwał, M.; Augustyn, M. Dispersion curves and identification of elastic wave modes for fiber metal laminates. *Compos. Struct.* **2021**, *255*, 112930. [CrossRef]
33. Rittmeier, L.; Losch, T.; Sinapius, M.; Lammering, R. Investigation on the influence of material interfaces and impedance changes on the propagation of guided waves in laminated steel layers. *Procedia Manuf.* **2018**, *24*, 196–202. [CrossRef]
34. Fattahi, A.; Shokrieh, M.M.; Kazemirad, S.; Ramezani, H. A guided wave propagation method for delamination detection in fiber-metal laminates. *Ultrasonics* **2024**, *142*, 107384. [CrossRef] [PubMed]
35. Moser, F.; Jacobs, L.J.; Qu, J. Modeling elastic wave propagation in waveguides with the finite element method. *NDT E Int.* **1999**, *32*, 225–234. [CrossRef]
36. Huo, H.; He, J.; Guan, X. A Bayesian fusion method for composite damage identification using Lamb wave. *Struct. Health Monit.* **2021**, *20*, 2337–2359. [CrossRef]

https://doi.org/10.3390/math14162961